# A specialized spinal circuit for command amplification and directionality during escape behavior

Na N. Guan[a,b,c,1], Lulu Xu[a,b,1], Tianrui Zhang[a,b], Chun-Xiao Huang[a,b], Zhen Wang[a,b], Elin Dahlberg[d], Haoyu Wang[e], Fangfang Wang[e], Irene Pallucchi[d], Yunfeng Hua[e,2], Abdeljabbar El Manira[d,2,3], and Jianren Song[a,b,c,d,2,3]

[a]Translational Research Institute of Brain and Brain-Like Intelligence, Shanghai Fourth People's Hospital, School of Medicine, Tongji University, Shanghai 200434, China; [b]Department of Anatomy, Histology, and Embryology, School of Medicine, Tongji University, Shanghai 200092, China; [c]Clinical Center for Brain and Spinal Cord Research, Tongji University, 200092 Shanghai, China; [d]Department of Neuroscience, Karolinska Institute, 171 77 Stockholm, Sweden; and [e]Shanghai Jiao Tong University School of Medicine, Ninth People's Hospital, Shanghai Institute of Precision Medicine, 200125 Shanghai, China

Edited by Eve Marder, Brandeis University, Waltham, MA, and approved August 25, 2021 (received for review April 9, 2021)

**In vertebrates, action selection often involves higher cognition entailing an evaluative process. However, urgent tasks, such as defensive escape, require an immediate implementation of the directionality of escape trajectory, necessitating local circuits. Here we reveal a specialized spinal circuit for the execution of escape direction in adult zebrafish. A central component of this circuit is a unique class of segmentally repeating cholinergic V2a interneurons expressing the transcription factor Chx10. These interneurons amplify brainstem-initiated escape commands and rapidly deliver the excitation via a feedforward circuit to all fast motor neurons and commissural interneurons to direct the escape maneuver. The information transfer within this circuit relies on fast and reliable axo-axonic synaptic connections, bypassing soma and dendrites. Unilateral ablation of cholinergic V2a interneurons eliminated escape command propagation. Thus, in vertebrates, local spinal circuits can implement directionality of urgent motor actions vital for survival.**

escape directionality | cholinergic V2a interneurons | spinal neural circuit | axo-axonic synapse

Vertebrates are endowed with a panoply of motor behaviors that are selected and executed as circumstances demand, allowing animals to thrive in a competitive environment (1–6). Movements need to be precisely directed for an action to achieve its intended goal. Therefore, an optimized system for selection of action direction can have an immediate impact on survival when facing a hazardous situation, such as a predator attack. Different circuits in the brain, especially the basal ganglia, control the selection and initiation of purposive actions, or sequences of actions, in a goal-directed manner (1, 7–9). The processing carried out by these circuits, however, may not be adequate for situations where accurate and near instantaneous selection of action direction is required, such as during escape from a predator (10–13). The circuits that implement such rapid behaviors need to be wired in a way to ensure accuracy, speed, and reliability of the motor action, and a precise control over its directionality.

The ability to move the whole body, or parts thereof, to the left or right is an essential action selection (14–16). In its simplest form, selection of action direction can be expressed by escape behavior (17, 18), which will lead to survival only if its directionality has been successfully implemented. In teleost fish, escape consists of a rapid bending of the body into a C-shape to orient away from a potential hazard, followed by a sequence of fast swimming (19–26), while suppressing the circuits for slow swimming (27). The escape sequence is triggered by sensory stimuli (auditory, visual, or tactile), which are rapidly transformed at the brainstem level into commands by the activation of the Mauthner cells (M-cells). The recruitment of feedforward inhibitory interneurons provides reciprocal inhibition among M-cells and has been suggested to ensure the directionality of escape (28, 29). However, bilateral firing of M-cells is known to occur during escape (30) and, therefore, the implementation of escape directionality might instead involve processing downstream of the M-cells, in the circuits of the spinal cord (30, 31). Anatomical and physiological studies in goldfish have characterized so-called spinal descending interneurons (32), which are activated exclusively by M-cells and in turn are electrically coupled to primary motor neurons (pMNs) (33). However, the precise identity and functional role of these interneurons is not known.

The genetic accessibility of zebrafish has enabled molecular identification of several interneuron classes (34). Among these are the excitatory V2a interneurons identified by their expression of the transcription factor Chx10 and distributed in the brainstem and spinal cord (34). Selective activation of these interneurons in the brainstem or spinal cord produces coordinated swimming activity (35, 36), while their restricted ablation in the spinal cord or silencing in brainstem inhibited swimming behavior (36, 37). Similarly, a global silencing of transmitter

## Significance

**We are constantly faced with a choice moving to the left or right; understanding how the brain solves the selection of action direction is of tremendous interest both from biological and clinical perspectives. In vertebrates, action selection is often considered to be the realm of higher cognitive processing. However, by combining electrophysiology, serial block-face electron microscopy, and behavioral analyses in zebrafish, we have revealed a pivotal role, as well as the full functional connectome of a specialized spinal circuit relying on strong axo-axonic synaptic connections. This includes identifying a class of cholinergic V2a interneurons and establishing that they act as a segmentally repeating hub that receives and amplifies escape commands from the brain to ensure the appropriate escape directionality.**

Author contributions: N.N.G., A.E.M., and J.S. designed research; N.N.G., L.X., E.D., F.W., Y.H., and J.S. performed research; N.N.G., L.X., and J.S. contributed new reagents/analytic tools; N.N.G., L.X., T.Z., C.-X.H., Z.W., H.W., I.P., Y.H., and J.S. analyzed data; and N.N.G., Y.H., A.E.M., and J.S. wrote the paper.

The authors declare no competing interest.

This article is a PNAS Direct Submission.



[1]N.N.G. and L.X. contributed equally to this work.

[2]To whom correspondence may be addressed. Email: yunfeng.hua@shsmu.edu.cn, abdel.elmanira@ki.se, or song.jianren@tongji.edu.cn.

[3]A.E.M and J.S. contributed equally to this work.

This article contains supporting information online at http://www.pnas.org/lookup/suppl/doi:10.1073/pnas.2106785118/-/DCSupplemental.

Published October 18, 2021.

release from all V2a neurons in the entire nervous system impaired swimming (38). In adult zebrafish, V2a interneurons form three interconnected modules that selectively drive slow, intermediate, and fast motoneurons to control the speed of locomotion (39). In larval zebrafish the connectivity of two types of V2a interneurons among themselves and primary motoneurons have been reported (40). These studies in both larval and adult zebrafish have focused on glutamatergic V2a interneurons and their role in controlling swimming at different speeds. It is thus still unclear if all V2a interneurons release glutamate or whether there are any nonglutamatergic types that are exclusively embedded within the escape spinal circuit.

In this study, we reveal a specialized spinal circuit that plays a pivotal role in generating the C-shape response to orient the body during escape in adult zebrafish. This includes a unique class of segmentally repeating excitatory cholinergic V2a interneurons, expressing the transcription factor Chx10 (esV2a), which represents a central component of this specialized circuit. These interneurons act as a segmental relay station that amplifies permissive escape commands from M-cells, and immediately distributes the excitation to all motor neurons innervating fast muscles, in turn generating the rapid C-shaped escape maneuver. In parallel, they ensure the directionality of escape by simultaneously engaging commissural local (CoLo) inhibitory interneurons, a neuron class that suppresses the activity of the contralateral neurons of this escape circuit. The detailed organization of this specialized circuit was established functionally using dual or triple whole-cell patch-clamp recordings and confirmed structurally by circuit reconstruction using three-dimensional electron microscopy. Furthermore, ablation of the cholinergic V2a interneurons on one side of the spinal cord obliterated the spread of the M-cell commands within the circuit and restricted the escape toward the intact side. Thus, the specialized circuit revealed in this study, with its central excitatory interneurons, plays a crucial role in amplifying and delivering the escape command to ensure an effective directionality of lateralized escape in a fast and timely manner. Conservation of brainstem–spinal organization across vertebrate classes suggests that homologous mechanisms play a similar role in directing urgent motor tasks in other vertebrates.

## Results

**Identification of a Cholinergic V2a Interneuron Population in the Escape Circuit.** While the majority of V2a interneurons are glutamatergic (34, 39–41), we now reveal a distinct cholinergic V2a interneuron type using two transgenic zebrafish lines. Using the Tol-056 enhancer trap line (42), we identified a specific type of interneuron located dorso-medially in the spinal cord that had its axon projecting toward the Mauthner axon (M-axon) suggesting a role in escape (Fig. 1 *A* and *B*). This candidate escape V2a (esV2a) interneuron expressed both choline acetyltransferase (ChAT) and the transcription factor Chx10 (Fig. 1 *A* and *B*), and on average, there was 1.1 ± 0.1 such interneuron per hemisegment (Fig. 1*C*) ($n = 16$ segments, 5 fish).

The existence of a cholinergic interneuron class expressing the transcription factor Chx10 was further confirmed using the *Chx10*:GFP transgenic line (34). Similar to the Tol-056 enhancer trap line, a dorso-medial interneuron expressing both ChAT and Chx10 was identified in the Tg(*Chx10*:GFP) line (Fig. 1 *D* and *E*), with an average distribution of 1.2 ± 0.1 per hemisegment (Fig. 1*F*) ($n = 16$ segments, 5 fish). To determine the molecular profile of the cholinergic esV2a interneurons, single identified interneurons were collected using a patch pipette and their molecular profile was determined using single-cell RNA sequencing. The collected interneurons showed a high expression of genes for the vesicular acetylcholine transporter slc18a3a (vacht), acetylcholine esterase (*ache*), choline O-acetyltransferase a (chata), and the transcription factor Chx10 (vsx2) (*SI Appendix*, Fig. S1).

The proximity of the axon of esV2a interneurons to the M-axon suggested that they may be part of the escape circuit. To determine if this was the case, we used the ex vivo adult zebrafish preparation (27, 43–45) in which escape and swimming circuits can be selectively activated (Fig. 1 *G* and *H*). Extracellular stimulation of the M-cell region in the brainstem produced a strong excitation that reached spiking threshold in esV2a interneurons recorded in Tol-056 (Fig. 1 *I* and *J*) or Tg(*Chx10*:GFP) zebrafish (Fig. 1 *K* and *L*). The chemical excitatory postsynaptic potential (cEPSP) from M-cells to this interneuron was blocked by the nicotinic acetylcholine receptor antagonist d-tubocurarine (50 μM), leaving only an electrical EPSP (eEPSP) in both transgenic lines ($n = 5$ for each case) (Fig. 1 *J* to *L*), confirming that M-cells are cholinergic (28). On the other hand, these interneurons were not recruited during swimming activity induced by stimulation of the rostral spinal cord, and displayed only small amplitude membrane potential oscillations (Fig. 1 *G*, *M*, and *N*).

The esV2a interneurons fired only a single action potential in response to prolonged depolarizing current pulses (Fig. 1 *I* and *K* and *SI Appendix*, Fig. S2*A*) and were less excitable than the glutamatergic V2a interneurons involved in swimming behavior (41, 46). They also had a more hyperpolarized resting membrane potential (~−70 mV), a relatively lower input resistance (~80 mΩ), and a higher rheobase (~1.6 nA) (*SI Appendix*, Fig. S2 *C–E*). Finally, esV2a interneurons in both transgenic lines showed near-identical morphologies with a small soma (85.7 ± 10.15 $\mu m^3$, $n = 22$) and extensive dendritic arborization, a thick descending axon projecting through three segments, and a thin ascending collateral extending locally within the segment where the soma resides (Fig. 1*O*).

These results identify a specialized interneuron class in adult zebrafish defined by a specific genetic profile and morphological features that is activated by escape, but not by swimming commands.

**esV2a Interneurons Are the Recipients of Escape Command.** The C-shape escape behavior induced by M-cell activation is considered to be mediated by a direct excitation of fast pMNs, and CoLo inhibitory interneurons that inhibit neurons on the contralateral side (12, 32, 42). However, given the effective excitation of esV2a interneurons by the M-cell, we next asked whether this population is in fact the first and primary responder to escape commands, and may function as a relay station to amplify, distribute, and coordinate the excitation of the other neurons in the escape circuit. This sequential transfer of escape command within the spinal circuit was revealed using triple whole-cell patch-clamp recordings made from an M-cell, an esV2a interneuron, and a pMN ($n = 8$) or a CoLo interneuron ($n = 7$). Current-injection activation of an M-cell action potential reliably elicited an action potential in the esV2a interneuron and the simultaneously recorded pMN or CoLo interneuron, which were reduced to eEPSPs after application of d-tubocurarine (Fig. 2 *A* and *B*), confirming that M-cells are cholinergic (28). However, in response to all M-cell action potentials, the action potentials in the esV2a interneuron always preceded the ones in the pMN and CoLo interneuron.

A detailed anatomical analysis of the simultaneously recorded M-cells, esV2a interneuron, pMN, and CoLo interneuron revealed putative sites of synaptic contacts ($n = 15$ for the esV2a interneuron, $n = 16$ for the pMN, and $n = 8$ for the CoLo interneuron). The recorded neurons were filled with neurobiotin and immunohistochemistry experiments were performed to determine the location of synaptic contacts. This also allowed us to confirm the identity of the recorded neurons based on their morphology and axonal projections. In all cases, esV2a interneurons

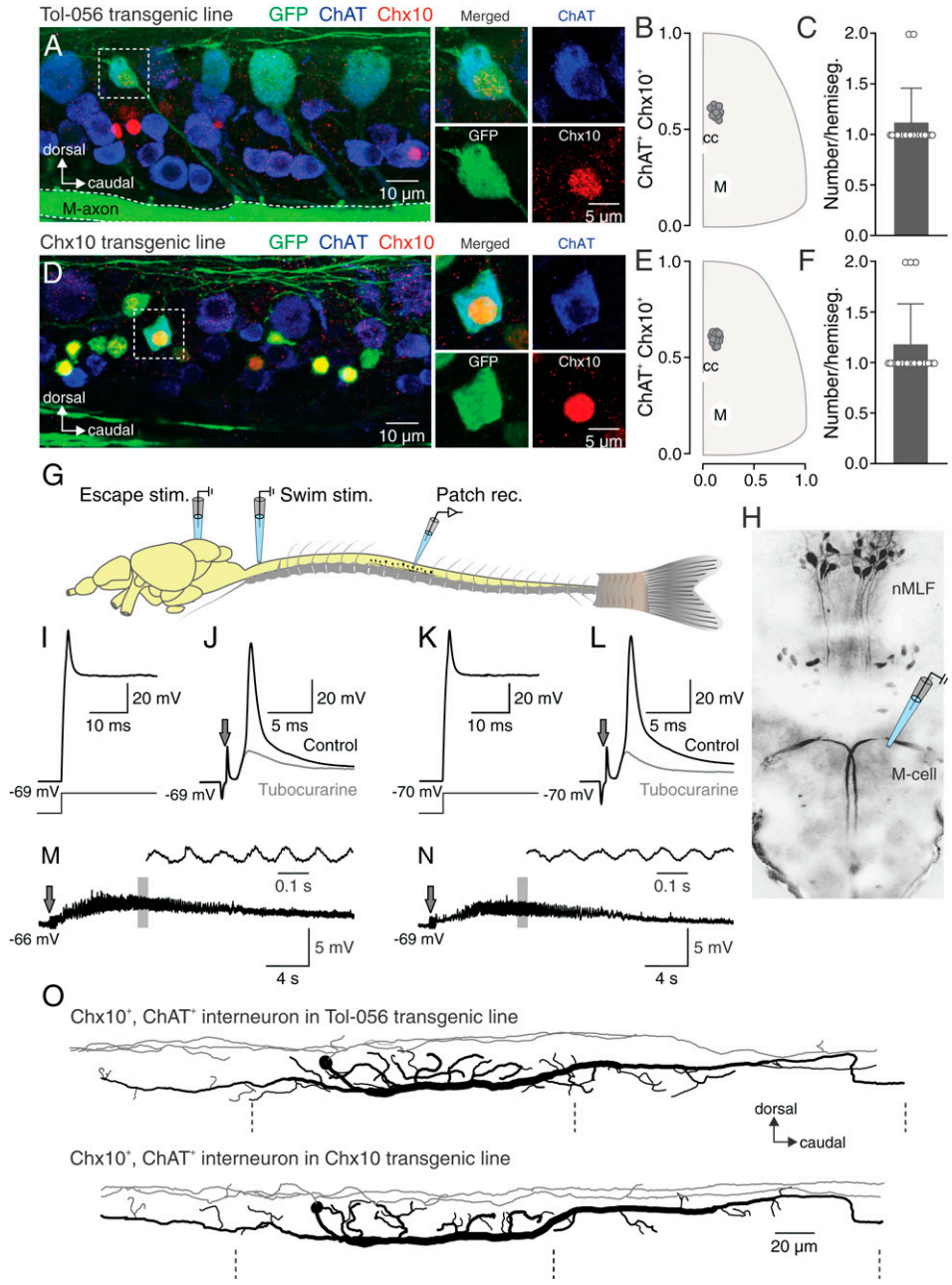


**Fig. 1.** esV2a interneurons involved in escape behavior. (*A*) Lateral view of a spinal segment from Tol-056 enhancer trap transgenic zebrafish line with immunohistochemical staining. The dashed box indicates a specific interneuron expressing GFP (green) that colocalizes both Chx10 (red) and ChAT (blue). This neuron is shown specifically on the right four boxes. (*B*) Distribution of esV2a interneurons in the spinal cord from the Tol-056 transgenic line (cc: central canal; M: M-axon). Data are from multiple fish and multiple segments. (*C*) Quantification of esV2a interneurons per hemisegment in Tol-056 transgenic line. The graph shows mean ± SD; $n = 16$. (*D*) Lateral view of a spinal segment from Tg(*Chx10*:GFP) transgenic line with immunohistochemical staining. A specific GFP expressing neuron (green) in the dashed box was immunoreactive for both Chx10 (red) and ChAT (blue) shown specifically in the right four boxes. Yellow represents noncholinergic V2a interneurons that express GFP (green) and Chx10 (red). (*E*) Distribution of esV2a interneurons in the spinal cord from Tg(*Chx10*:GFP) transgenic line (cc: central canal; M: M-axon). (*F*) Quantification of esV2a interneurons per hemisegment in Tg(*Chx10*:GFP), the graph shows mean ± SD; $n = 16$. (*G*) Experimental setup of the ex vivo preparation showing the sites for extracellular stimulation and whole-cell patch-clamp recordings. (*H*) Dorsal view of descending neurons in the zebrafish hindbrain revealed by retrograde labeling from the spinal cord. (*I*) esV2a neuron in Tol-056 transgenic line discharged a single action potential in response to a prolonged depolarizing current injection. (*J*) The same esV2a neuron as in *I*, receiving a strong cholinergic cEPSP from an M-cell that was blocked by d-tubocurarine leaving on an eEPSP. Arrow indicates electrical stimulation. (*K*) An esV2a neuron in Tg(*Chx10*:GFP) firing a single action potential in response to a prolonged depolarizing current injection. (*L*) The same esV2a neuron as in *K* receiving a strong cholinergic cEPSP by an M-cell stimulation that was blocked by d-tubocurarine leaving only an eEPSP. Arrow indicates electrical stimulation. (*M*) An esV2a interneuron recorded in the Tol-056 line was not recruited during swimming activity (same interneuron as in *I* and *J*). Arrow indicates electrical stimulation. (*N*) An esV2a interneuron recorded in the Tg(*Chx10*:GFP) line was not recruited during swimming activity (same interneuron as in *K* and *L*). Arrow indicates electrical stimulation. (*O*) Morphology of an esV2a neuron in Tol-056 line (*Upper*) and Tg(*Chx10*:GFP) (*Lower*). Gray line representing the dendrite and black representing the soma and axonal projections. The dashed lines indicating the segmental boundaries.

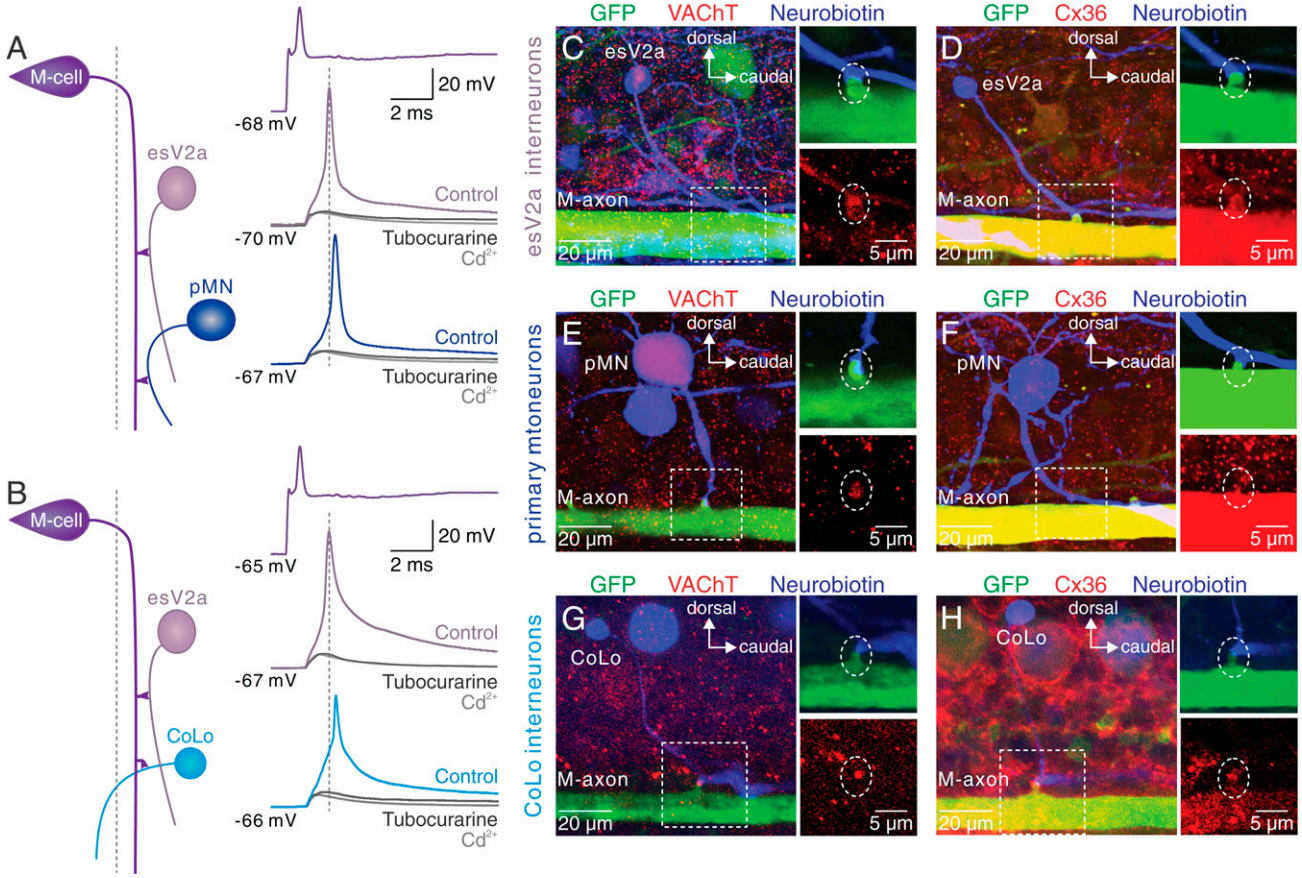


**Fig. 2.** esV2a interneurons are recruited prior to pMNs and CoLo interneurons. (*A*) Triple whole-cell patch-clamp recording from an M-cell, an esV2a interneuron and a pMN. M-cell activation recruited first the esV2a interneuron and then the pMN. d-tubocurarine suppressed the firing of both neurons and only a $Cd^{2+}$-insensitive eEPSP remained. (*B*) Triple whole-cell patch-clamp recording from an M-cell, an esV2a interneuron and a CoLo interneuron. The latter was recruited later than the esV2a interneuron. The cholinergic cEPSPs in both neurons were blocked by d-tubocurarine, leaving only an eEPSP remained that was unaffected by $Cd^{2+}$. (*C*) Direct contact between the M-axon (green) and the axon of an esV2a interneuron (blue). VAChT (red) was expressed at the site of presumed synaptic contact (dashed box, *Left*). The large soma corresponds to a pMN expressing GFP in this line. (*D*) Expression of Cx36 (red) at the site of synaptic connections between the M-axon and esV2a interneuron (blue). (*E*) The expression of VAChT (red) was found at the presumed synaptic contact site between an M-axon (green) and a pMN (blue). (*F*) Cx36 (red) is expressed at the connection site between the M-axon and pMN. (*G*) The expression of VAChT (red) was found at the presumed synaptic contact site between an M-axon (green) and a CoLo interneuron (blue). (*H*) Expression of Cx36 (red) at the connection site between the M-axon and CoLo interneuron. The *Right Upper* and *Lower* panels in *C–H* represent magnification of the regions indicated by the dashed boxes in the *Left* panels. The white dotted circle indicates the synapses formed by the M-cell and spinal neurons.

displayed ipsilateral axonal projections, while CoLo interneurons projected locally to the contralateral side of the spinal cord. The putative synaptic contacts between the M-axon and the esV2a/CoLo/pMN always occurred at the axo-axonic level at sites where collateral buds emerged from the main M-axon. Confocal imaging stacks showed that the M-axon buds formed putative synapses with the axons of the esV2a interneuron (Fig. 2 *C* and *D*), the pMN (Fig. 2 *E* and *F*), and the CoLo (Fig. 2 *G* and *H*). These apparent synaptic sites expressed both vesicular acetylcholine transporter (VAChT) and connexin 36 (Cx36), further supporting the existence of direct synaptic contacts between M-axon and these three neuronal classes within the spinal escape circuit. Similar to esV2a interneurons, CoLo interneurons also fired only a single action potential in response to a depolarizing current pulse and had a relatively hyperpolarized resting-membrane potential (*SI Appendix*, Fig. S2 *B* and *C*), but they exhibited a higher input resistance and a lower rheobase than esV2a interneurons (*SI Appendix*, Fig. S2 *D* and *E*). The identity of CoLo interneurons was also examined using single-cell RNA sequencing. The results showed high gene expression for the transcription factor *dmrt3*, vesicular glycine transporters slc6a5 (*GlyT2*), and slc6a9 (*GlyT1*) (*SI Appendix*, Fig. S3).

Together these results support a sequential transfer of escape command. While all components of the spinal escape circuit receive direct synaptic contacts from the M-axon, the esV2a interneurons are the first responders, suggesting that they act as a relay station to amplify and instantly distribute escape command to pMNs and CoLo interneurons to implement the C-shape escape.

**Ablation of esV2a Interneurons Impairs Direction of Escape.** To examine if the esV2a interneurons indeed play a critical role in amplifying and distributing M-cell commands within the escape circuit, we performed ablation experiments in vivo and ex vivo. The effect of stimulating an M-cell on pMNs, secondary fast MNs (fMNs), and CoLo interneurons was examined before and after esV2a interneurons were ablated (Fig. 3*A*). Dual whole-cell patch-clamp recordings were made ex vivo from an M-cell and a pMN, fMN, or CoLo interneuron (Fig. 3*B*). Before esV2a ablation (control), an action potential induced in an M-cell by depolarizing their membrane potential resulted in firing of an action potential in the simultaneously recorded pMNs, fMNs, or CoLo interneurons ($n = 7$ for each group) (Fig. 3 *B* and *C*). After two-photon laser ablation of four to five spinal esV2a interneurons across three to four spinal segments rostral to the recorded neurons, the same M-cell stimulation

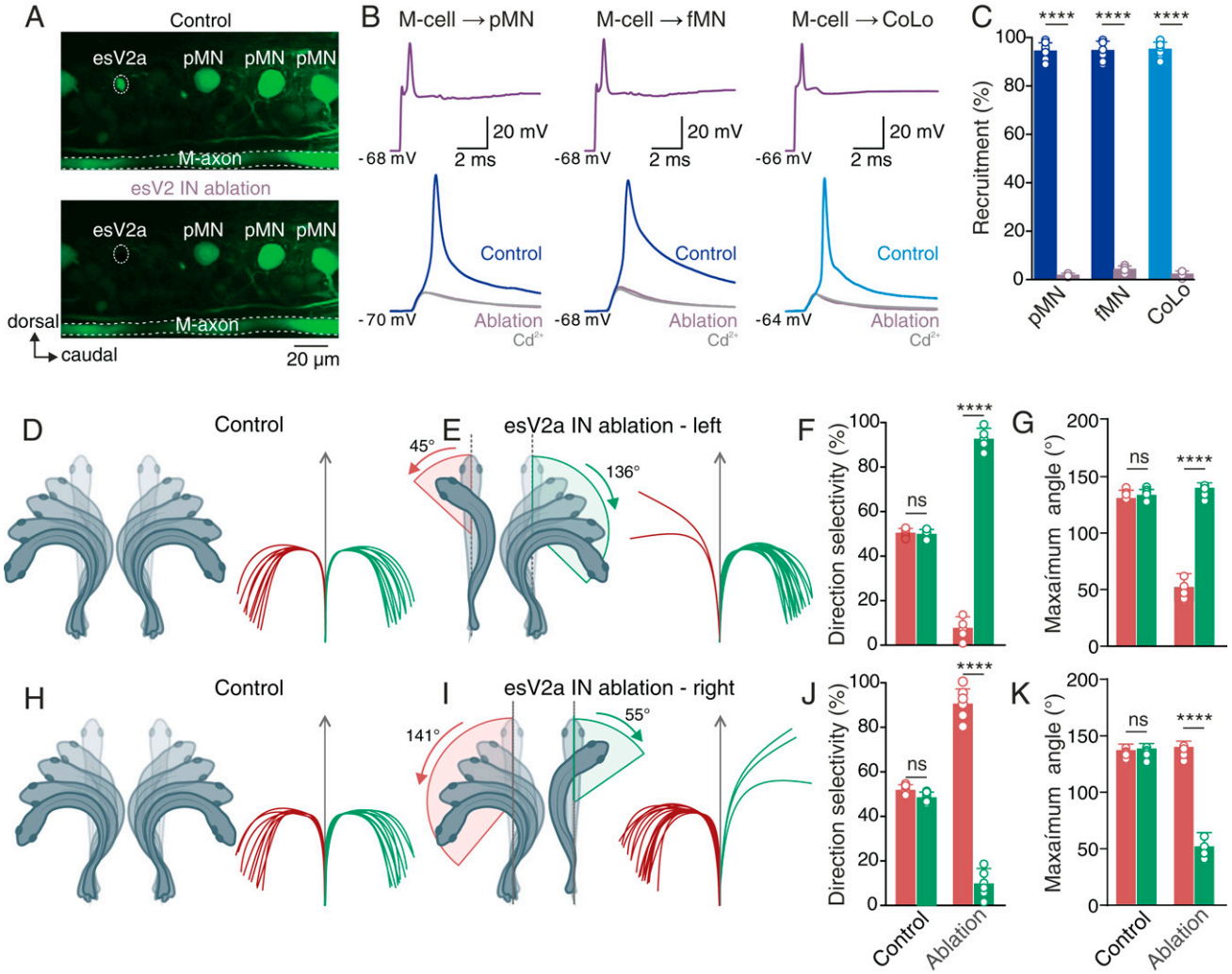


**Fig. 3.** Ablation of spinal esV2a interneurons suppresses the transmission of the escape command and the behavioral laterality in vivo. (*A*) Two-photon microscope images of the spinal cord before (*Upper*) and after laser ablation (*Lower*) of an esV2a interneuron. (*B*) Ablation of esV2a interneurons eliminated the ability of the M-cell to elicit an action potential in a pMN, an fMN, and a CoLo interneuron. Only direct electrical transmission from the M-cell remained and was unaffected by $Cd^{2+}$. (*C*) Quantification of the probability of recruitment of pMNs, fMNs, and CoLo interneurons before and after esV2a interneuron ablation. Graph shows mean ± SD, $n = 7$ each; Student's *t* test, $P = 1 \times 10^{-7}$ for pMN, $P = 8 \times 10^{-6}$ for fMN, and $P = 6 \times 10^{-7}$ for CoLo. Each dot represents the data from single neurons. (*D*) In freely behaving zebrafish in vivo, the direction of escape behavior was flexible in response to a brief sound stimulation from a constant source location. Zebrafish produced escape behavior directed toward both directions. (*E*) In animals with ablation of esV2a interneurons on the left side of spinal cord, escape was almost exclusively directed toward the intact side of the spinal cord. The maximum body bending angle was shallower toward the ablated side. (*F*) Quantification of the directional selectivity of escape behavior before and after esV2a interneuron ablation. Data in the graph represent mean ± SD; Student's *t* test, $P > 0.5$ for control; $P = 4 \times 10^{-5}$ for ablation, $n = 8$ for each group. (*G*) Maximum body bending angle in control and in ablated fish. Data in the graph represent mean ± SD; Student's *t* test, $P > 0.5$ for control; $P = 9 \times 10^{-5}$ for ablation, $n = 8$ for each group. (*H*) Control zebrafish were able to escape in both direction in response to sound stimulation. (*I*) After ablation of esV2a interneurons on the right side of spinal cord, the direction of escape was confined toward the intact side of the spinal cord. (*J*) Quantification of the directionality of escape before and after esV2a interneuron ablation. Data in the graph represent mean ± SD; Student's *t* test, $P > 0.5$ for control; $P = 3 \times 10^{-6}$ for ablation, $n = 7$ for each group. Each dot represents the data from single animals. (*K*) Maximum body bending angle in control and in ablated fish. Data in the graph represent mean ± SD; Student's *t* test, $P > 0.5$ for control; $P = 8 \times 10^{-6}$ for ablation, $n = 7$ for each group. Each dot represents the data from single animals. The red and green traces in *D–L* represent tracking of sound induced escape in all the 20 trials in a single fish; right and left directions are represented as green and red, respectively.

failed to produce any action potentials in pMNs, fMNs, and CoLo interneurons (Fig. 3 *B* and *C*). In all cases, only an eEPSP was elicited by M-cell stimulation that was not affected by $Cd^{2+}$ (100 µM; $n = 7$ for each group) (Fig. 3*B*). These results indicate that the escape command from M-cells is relayed via chemical synapses from the esV2a interneurons to pMNs, fMNs, and CoLo interneurons.

The critical role of esV2a interneurons for escape direction selectively was tested in vivo. For this we performed behavioral experiments during which escape was induced by sound stimulation in control animals and in animals in which 20 to 25 esV2a interneurons were ablated unilaterally. In control animals, escape behavior did not display any direction preference. These animals displayed a flexible escape direction and were able to produce body bends directed either to the left or to the right in response to sound stimulation ($n = 7$ for each group) (Fig. 3 *D* and *G*). In animals in which esV2a interneurons were ablated on the left (Fig. 3 *E* and *F*) or the right (Fig. 3 *I* and *J*) side of the body, there was a loss of the flexibility of escape trajectory. Instead, these animals showed a directional bias of body bend

during escape toward the nonablated side. In a few trials (~2 of 20 trials), fish moved toward the ablated side with a shallow angle (Fig. 3 *E*, *G*, *I*, and *K*). In sham ablation experiments, in which the same number of nonesV2a interneurons were ablated, there was no directionality bias during escape behavior (*SI Appendix*, Fig. S4 *A–C*). Furthermore, ablation of esV2a interneurons did not affect swimming activity, which could still be induced in the same preparations by stimulating descending axons and recorded in fMNs ex vivo (*SI Appendix*, Fig. S4*D*). These results demonstrate that esV2a interneurons represent a central component of the spinal escape circuit; they amplify and quickly relay escape commands from M-cells to all components of the circuit to rapidly initiate the behavior and ensure its flexible trajectory. The esV2a feedforward excitation of pMNs, fMNs, and CoLo interneurons is indispensable for the recruitment of the whole spinal escape circuit and, hence, allows animals to implement proper escape trajectory to avoid danger.

**Wiring Diagram of the Spinal Escape Circuit.** To better understand the information flow of the escape command within the spinal escape circuit, we imaged one whole spinal segment in an 8-wk-old zebrafish using serial block-face electron microscopy (SBEM) (47–50). The acquired SBEM volume was 251.4 × 187.7 × 248.3 $\mu m^3$ at a voxel size of 12 × 12 × 35 $nm^3$ (Fig. 4*A* and Movie S1), which allows a dense connectome reconstruction of the spinal escape circuit by skeletonizing the neurites and annotating the synapses (Fig. 4 *A* and *B*). M-axons were heavily myelinated, with regular myelin gaps where collateral buds extended to form synapses with neurons of the escape circuit (Fig. 4 *B–F* and Movies S1 and S2). After reconstructing the synaptic connections from the presynaptic M-axons and the morphology of the postsynaptic neurons, a complete circuit motif was revealed. Ten presynaptic M-axon collaterals and three different neuronal types were identified and analyzed. Twelve synapses were identified that evenly distributed on both the left and the right sides of a spinal segment (Fig. 4*B* and *SI Appendix*, Fig. S5 *A* and *B*). Based on their morphological features, spatial location, and synaptic contacts with M-axon collateral buds, the postsynaptic neurons were identified as the three neuronal populations of the spinal escape circuit: the two esV2a interneurons (one on each side of the spinal cord: L-esV2a and R-esV2a) displaying an ipsilateral descending axonal projection, two CoLo interneurons (one on each side of the spinal cord: L-CoLo and R-CoLo), and eight pMNs (four on each side of the spinal cord: L-pMN1 to -4 and R-pMN1 to -4) with their axon projecting to the ipsilateral ventral root (Fig. 4 *B* and *C* and *SI Appendix*, Fig. S5 *A* and *B*).

Among five M-axon collateral buds on each side, four made single axo-axonic synaptic contacts with either a CoLo interneuron or three different pMNs, while the fifth one made contact with both esV2a and pMN either on the left (L-esV2a and L-pMN1) or on the right (R-esV2a and R-pMN2) side of the spinal cord (Fig. 4 *B–D* and *SI Appendix*, Figs. S5*A* and S6*A*, *Left*). The ultrastructure of the M-axon synapses with the spinal escape neurons showed clear differences (Fig. 4 *D–F* and *SI Appendix*, Fig. S6 *A* and *B* and Movies S3 and S4). The M-axon presynaptic terminals targeting the esV2a interneurons contained synaptic vesicle clouds in proximity to the presynaptic membrane (Fig. 4*D*, green arrow). However, virtually no synaptic vesicles were present at the presynaptic terminals targeting pMNs and CoLo interneurons (Fig. 4 *D–F* and *SI Appendix*, Fig. S6, green arrows). To further quantify the differential distribution of vesicles at the presynaptic boutons connected to the esV2a interneurons and pMNs, we measured the distance from synaptic vesicles to the presynaptic membrane (putative active zone) (Fig. 4*H*). The distance of the 30 nearest vesicles to the presynaptic membrane was much shorter in synapses onto esV2a (L-esV2a: 75.8 ± 17.2 nM; R-esV2a: 51.9 ± 13.9 nM) compared to those onto pMNs (L-pMN1:252.5 ± 21.5 nM; R-pMN2: 209.1 ± 35.9 nM) (Fig. 4 *G* and *H*). These results, together with the electrophysiology data, support the fact that the M-cell connects to esV2a interneurons with mixed electrical and chemical synapses, while it only connects pMNs and CoLo interneurons via gap junctions.

The complete wiring diagram of the spinal escape circuit was reconstructed using skeleton tracing of esV2a interneurons, CoLo interneurons, pMNs, and fMNs (Fig. 4 *B*, *C*, *I*, and *J*). The esV2a interneurons made synaptic connections with the CoLo interneurons, pMNs, and fMNs at variable subcellular locations (Fig. 4*I* and *SI Appendix*, Fig. S5*B*). Synaptic vesicle clouds were always found prevalent in all presynaptic esV2a boutons to the CoLo interneurons, pMNs, and fMNs (Fig. 4*I*), arguing for functional chemical transmission. Moreover, single esV2a interneuron synaptic contacts with pMNs and fMNs were approximately two- to fivefold more frequent than those from the M-axon (*SI Appendix*, Fig. S5 *A* and *B*). On the other hand, CoLo interneurons made chemical synaptic contact only with the contralateral esV2a interneurons and pMNs, but not with fMNs (Fig. 4*J* and *SI Appendix*, Fig. S5*D*). These results indicate that the esV2a interneurons make widespread synaptic contacts with all components of the escape circuit (Fig. 4*I* and *SI Appendix*, Fig. S5*B*), while the CoLo interneurons only target contralateral esV2a interneurons and pMNs, which are exclusively active during escape, but not fMNs engaged both during escape and swimming (Fig. 4*J* and *SI Appendix*, Fig. S5*C*).

These results, together with the above electrophysiology data, reveal a quantitative wiring diagram of the spinal escape circuit and highlight how the escape command is first relayed to esV2a interneurons before it is transmitted to the rest of the circuit. They also suggest that esV2a interneurons act as a relay station to amplify and propagate escape commands and hence play a pivotal role in implementing escape behavior.

**esV2a Interneurons Act as a Central Excitatory Relay for Escape Commands.** Rapid escape is mediated by activation of fast muscles, which are innervated by the secondary fMNs in addition to pMNs. The above-described connectivity map shows that the esV2a interneurons are an essential excitatory relay station for the M-cell command to pMNs and fMNs to produce escape and determine its directionality. To functionally confirm the synaptic connections revealed by SBEM connectomics, dual whole-cell patch-clamp recordings were performed from esV2a interneurons and pMNs or fMNs (Fig. 5). pMNs received both electrical and chemical synaptic inputs from the esV2a interneurons (Fig. 5 *A* and *B*). The chemical component of the EPSPs was blocked by d-tubocurarine (50 μM; $n$ = 7), leaving an eEPSP that persisted following bath application of $Cd^{2+}$ (100 μM; $n$ = 7). The existence of dye-coupling between an esV2a interneuron and two pMNs was also revealed by neurobiotin injection (*SI Appendix*, Fig. S7*D*). Reconstructions of the recorded neurons revealed close axo-axonic appositions between the esV2a interneurons and pMNs that colocalized with the VAChT ($n$ = 4 of 4 preparations) (Fig. 5*C*). The excitation from esV2a interneurons was not limited to pMNs located in the same segment but was also spread to pMNs in more caudal segments (Fig. 5 *D* and *E*). However, the strength of excitation was higher in pMNs in the same segment compared to those in caudal segments (Fig. 5 *D* and *E* and *SI Appendix*, Fig. S7 *A–C*).

The excitation from esV2a interneurons to fMNs was also mediated by mixed electrical and chemical synapses (Fig. 5 *F* and *G*). However, unlike the esV2a connection with pMNs, a single action potential in the presynaptic interneurons was sufficient to produce a large EPSP in fMNs that reached firing threshold ($n$ = 11) (Fig. 5*G*). There was thus a one-to-one relationship between the pre- and postsynaptic action potentials (Fig. 5*G*). Both the EPSPs and the resulting action potentials were blocked by d-tubocurarine (50 μM; $n$ = 11) (Fig. 5*G*), and

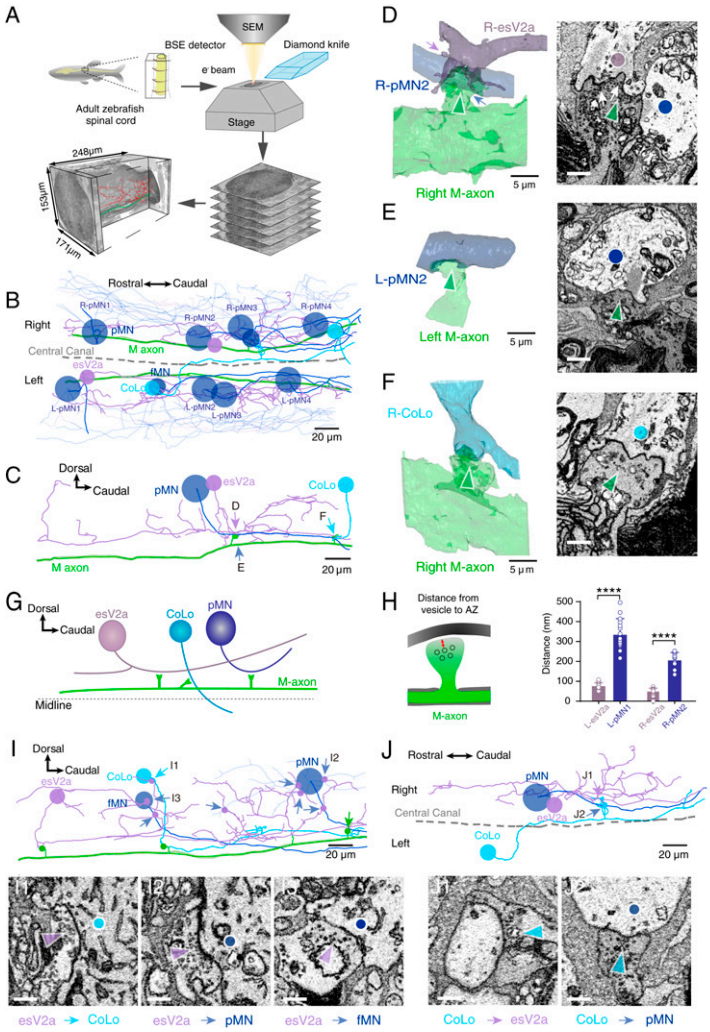


**Fig. 4.** Connectome of spinal escape neural circuit revealed by SBEM. (*A*) Workflow of acquiring three-dimensional electron microscopy volume from adult zebrafish spinal cord. The images were centered at the central canal and covered the entire spinal cord cross-section; 7,095 cuts along the axial direction were performed, resulting in a final dimension of 171 × 153 × 248 μm$^3$. Skeletonized reconstruction was done by human annotations. (*B*) Skeletonized neurites of eight pMNs (navy blue, larger soma size), two esV2a interneurons (purple), two CoLo interneurons (sky blue), two fMNs (navy blue, smaller soma size), as well as two M-axons (green) contained in the dataset. Dashed line indicating the spinal central canal. (*C*) The contralateral view of connectomes of the right M-axon (green), R-esV2a interneuron (purple), R-pMN2 (navy blue), and R-CoLo (sky blue) in the right side of the spinal cord. The collateral of M-axon made putative axo-axonal synaptic contacts with the R-esV2a interneuron (purple), the R-pMN2 (navy blue), and the R-CoLo interneurons (sky blue). (*D*) Volume reconstruction (*Left*) and electron micrographs (*Right*) of the indicated synaptic contacts in *C* (purple and navy blue arrow). The second collateral of the right M-axon made synaptic contacts with both the R-esV2a interneuron and the R-pMN2. Vesicle cluster (indicated by white arrows) in the terminal of the M-axon collateral (*Right*, green arrow) was found in the vicinity of the R-esV2a interneuron (*Right*, purple dot), but not of the pMN2 (*Right*, navy blue dot). (*E*) Volume reconstruction (*Left*) and electron micrograph (*Right*) of the indicated synaptic contact. The third collateral of the left M-axon made synaptic contacts with axon of a L-pMN2. No vesicle cluster in the terminal of M-axon collateral (*Right*, green arrow) was found in the vicinity of the L-pMN1 axon (*Right*, navy blue dot). (*F*) Volume reconstruction (*Left*) and electron micrograph (*Right*) of the indicated synaptic contacts in *C*. The fifth collateral of the right M-axon made synaptic contacts with the R-CoLo interneuron. No vesicle cluster in the terminal of right M-axon collateral (*Right*, green arrow) was found in the vicinity of the R-CoLo axon (*Right*, sky blue dot). (*G*) The wiring diagram between right M-axon with the three types of spinal interneurons in the right side of the spinal cord. M-axon formed putative synapses with the esV2a interneurons, the CoLo interneuron and pMNs. (*H*, *Left*) The drawing showing the distance between vesicles and presynaptic membrane. (*Right*) Statistic results suggest the different distance for esV2a interneurons and pMNs (Student's *t* test, $n = 30$; $P = 1 \times 10^{-6}$ for L-esV2a and L-pMN1; $n = 30$; $P = 5 \times 10^{-5}$ for R-esV2a and R-pMNs). Each dot represents the data from single vesicles. (*I*) Lateral view of connectomes of a presynaptic L-esV2a interneuron (purple) with a postsynaptic L-CoLo interneuron (sky blue), L-pMN4 (navy blue), and L-fMN (navy blue) on the left side of spinal cord in *B*. Chemical synapses (purple dots) were formed between the axon of presynaptic L-esV2a interneuron and the axon of the postsynaptic L-CoLo interneuron (sky blue), L-pMN4 (navy blue, larger soma size), and L-fMN (navy blue, smaller soma size). Electron micrographs (*I1*, *I2*, and *I3*) showing the indicated synaptic contacts. Colored arrows indicating the location and standing for the neuronal types. (*J*) Connectomes of a presynaptic L-CoLo interneuron with a postsynaptic R-esV2a interneuron (purple) and a postsynaptic R-pMN2 (navy blue) on the contralateral side of spinal cord in the dorsal view. The presynaptic L-CoLo interneuron made axo-axonic synapses (sky blue dots) with the contralateral pMN (navy blue) and cholinergic esV2a interneuron (purple). Electron micrographs (*J1* and *J2*) showing the indicated synaptic contacts. Colored arrows indicating the location and standing for the neuronal types. (Scale bars in *B*, *C*, *I*, and *J*: 20 μm; in *D–F*, *Left*: 5 μm; *D–F*, *Right*: 500 nm; and in *I1* to *I3* and *J1* and *J2*: 500 nm.)

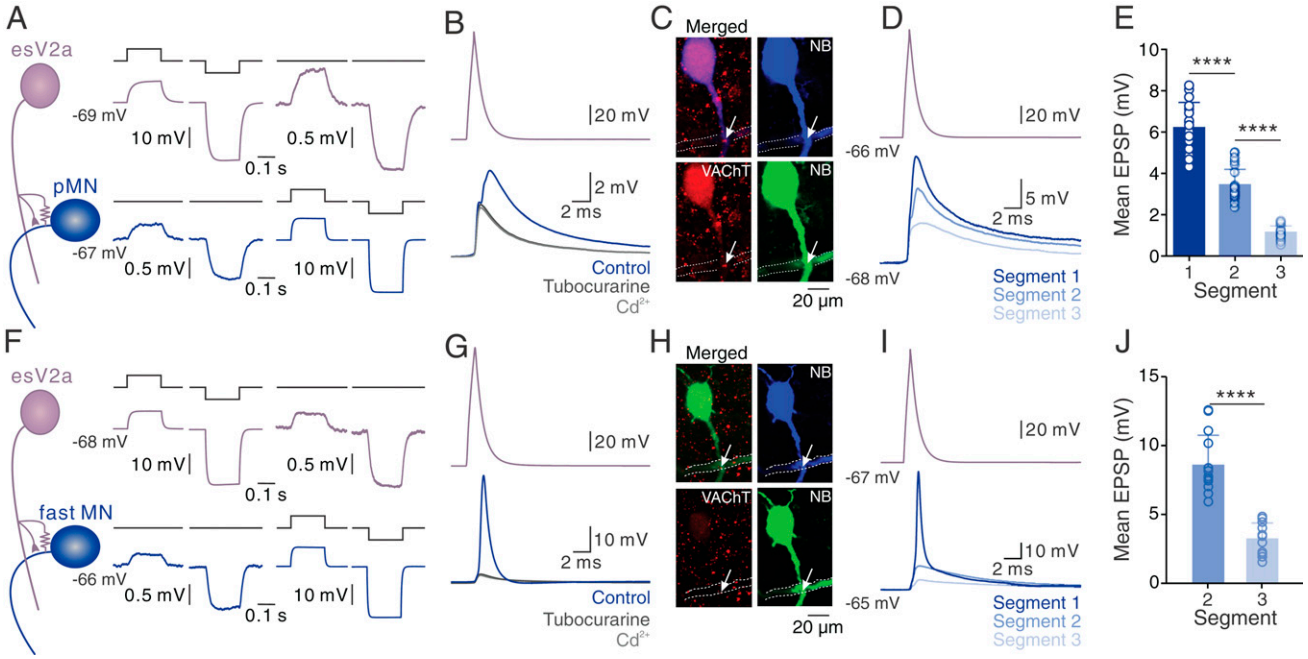


**Fig. 5.** esV2a interneurons drive ipsilateral escape MNs. (*A*) Dual whole-cell patch-clamp recording from an esV2a interneuron and a pMN connected via bidirectional electrical coupling. (*B*) Stimulation of the esV2a interneuron induced monosynaptic EPSPs in the pMN whose chemical component was blocked by d-tubocurarine, leaving only the $Cd^{2+}$-insensitive eEPSP. (*C*) Confocal images showing VAChT (red) expressing at the crossing site (white arrow) between the axon of the esV2a interneuron (dashed line) and the pMN (blue); same neurons as in *B*. The green channel is the same as the blue channel and represents a pseudocoloring of neurobiotin filled neurons for better visibility. (*D*) The EPSP amplitude was highest in the pMN in the same segment as the esV2a interneuron and decreased in more caudal segments. (*E*) Quantification of the mean EPSP amplitude based on the segmental location of the pMNs relative to the recorded esV2a interneuron (each bar represents mean ± SD, segment 1: $n = 16$; segment 2: $n = 15$; segment 3: $n = 12$; one-way ANOVA, $P = 2 \times 10^{-5}$ for segment 1 vs. segment 2; $P = 0.5 \times 10^{-6}$ for segment 2 vs. segment 3). Each dot represents the data from single neurons. (*F*) Dual whole-cell patch-clamp recording between an esV2a interneuron and a fMN showing bidirectional electrical coupling. (*G*) Single action potential in an esV2a interneuron induced an action potential in a caudal fMN that was blocked by d-tubocurarine leaving only an eEPSP that was unaffected by $Cd^{2+}$. (*H*) Confocal images showing VAChT (red) expressing at the crossing site (white arrow) between the axon of the esV2a interneuron (dashed line) and the fMN (blue); same neurons as in *G*. The green channel is the same as the blue channel and represents a pseudocoloring of neurobiotin filled neurons for better visibility. (*I*) The EPSP in fMN in the same segment as the esV2a interneuron was highest and reached firing threshold, and it decreased in fMNs located in more caudal segments. (*J*) Quantification of the mean EPSP amplitude amplitude based on the segmental location of the fMNs relative to the recorded esV2a interneuron (each bar represents mean ± SD, segment 1: $n = 15$; segment 2: $n = 10$; segment 3: $n = 9$; paired *t* test, $P = 0.3 \times 10^{-5}$ for segment 2 vs. segment 3). EPSPs in fMNs in segment 1 could not be quantified because they were always suprathreshold. Each dot represents the data from a single neuron.

only the eEPSP remained in $Cd^{2+}$ (100 μM $n = 11$) (Fig. 5*G*). The synaptic contact between the presynaptic esV2a interneurons and postsynaptic fMNs occurred at the axo-axonic level and was defined by the expression of VAChT ($n = 3$ of 3 preparations) (Fig. 5*H*). The excitation was spread to fMNs in more caudal segments, with a gradual decrease in strength in successively more caudal segments (Fig. 5 *I* and *J*). However, esV2a interneurons did not make synaptic contacts with slow MNs ($n = 10$) (*SI Appendix*, Fig. S7*E*), which are known to be active only during swimming (51).

As predicted by the connectome, these results show that the esV2a interneurons provide a widespread excitatory drive to pMNs and fMNs innervating fast muscles underlying escape. Hence, the esV2a interneurons appear to play an important role in amplifying the escape command and relaying it nearly instantaneously to produce escape behavior.

**esV2a Interneuron Feedforward Circuit Relays Escape Commands.** To determine if ipsilateral esV2a interneurons are interconnected, dual whole-cell patch-clamp recordings were performed (Fig. 6*A*). All recorded interneurons were connected, with bidirectional electrical coupling via gap junctions (Fig. 6*A*). However, chemical synaptic transmission was unidirectional from the rostral to the caudal interneurons (Fig. 6*B*). Stimulation of rostral interneurons elicited EPSPs in the caudal ones whose transmitter-mediated component was blocked by d-tubocurarine (50 μM), leaving only an eEPSP that remained unchanged in the presence of $Cd^{2+}$ (100 μM; $n = 6$) (Fig. 6 *B* and *C*). The strength of excitation was highest to esV2a interneurons in the adjacent segment (*SI Appendix*, Fig. S8 *A* and *B*). In contrast, stimulation of the caudal esV2a interneurons induced only an electrical response in the rostral interneurons that was not affected by application of d-tubocurarine and $Cd^{2+}$ ($n = 6$) (Fig. 6 *B* and *C*). The recorded interneurons were filled with neurobiotin and reconstructed using confocal microscopy to reveal close appositions that colocalized with both connexin 36 and VAChT ($n = 2$ of 2 preparations) (Fig. 6*D*). These results suggest that the esV2a interneurons form a feedforward excitatory circuit that promotes the amplification and spread of the excitatory command in a manner that is necessary for the execution of escape behavior with its unidirectional rostro-caudal propagation along the body.

A prerequisite for the execution and directional selectivity of escape behavior is that all MNs innervating fast muscles are immediately recruited. Our results show that there was a one-to-one recruitment from esV2a interneurons to fMNs, but only subthreshold responses were elicited in pMNs by activation of single interneurons. To determine if the converging excitation from numerous esV2a interneurons is sufficient to recruit pMNs, triple whole-cell patch-clamp recordings were made from two esV2a interneurons and a pMN ($n = 13$) (Fig. 6*E*). Stimulation of each esV2a interneuron alone produced only subthreshold response in the pMN (Fig. 6 *E* and *F*). However,

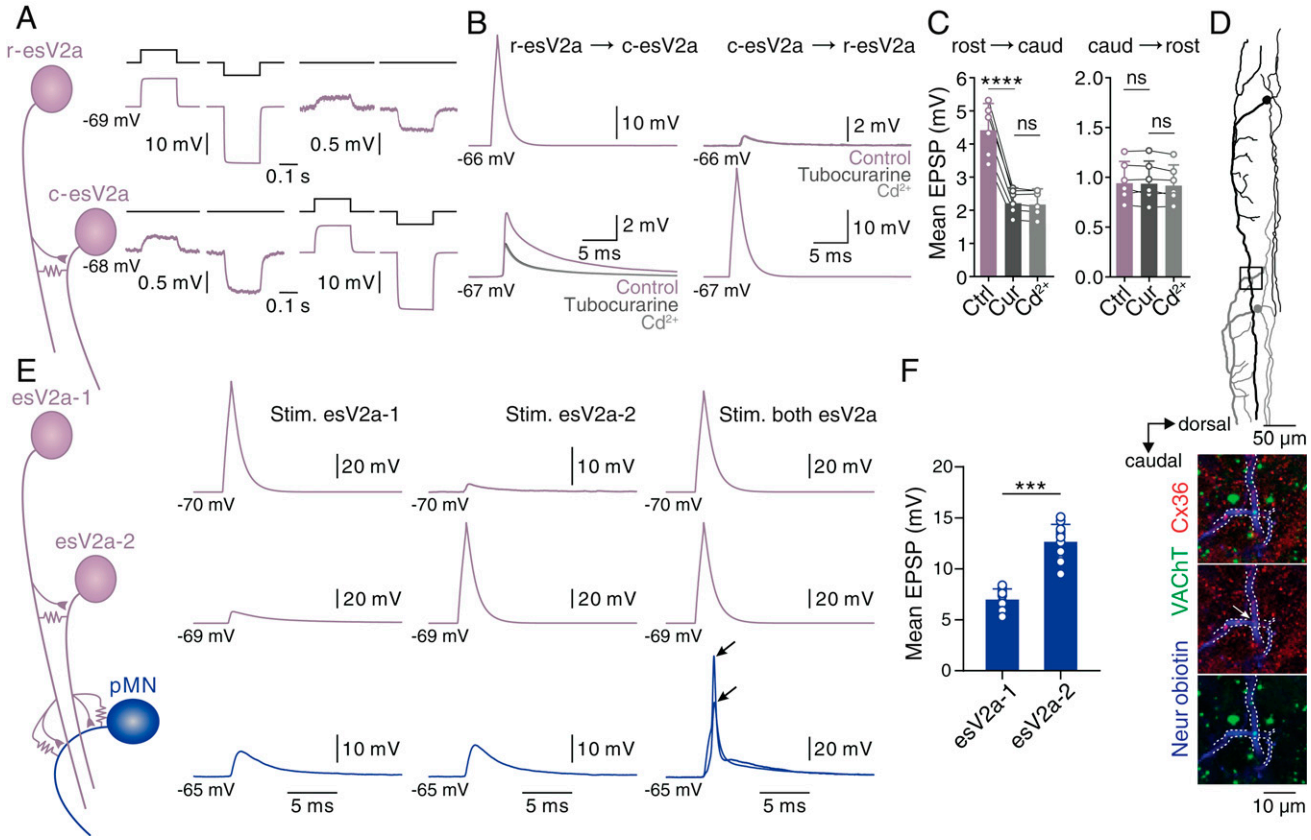


**Fig. 6.** Feedforward excitation between esV2a interneurons and convergence onto pMNs. (*A*) Dual whole-cell patch-clamp recording from a rostral and a caudal esV2a interneuron that were electrically coupled. (*B*) Chemical synaptic transmission occurred only from the rostral to the caudal esV2a interneuron. (*C*) Quantification of the mean amplitude of synaptic potentials between esV2a interneurons. The *Left* graph represents data from rostral to caudal esV2a interneuron as mean ± SD, $n = 6$; one-way ANOVA, $P = 6 \times 10^{-6}$ for control vs. d-tubocurarine (Cur); $P > 0.05$ for d-tubocurarine vs. $Cd^{2+}$. The *Right* graph represents data from caudal to rostral esV2a interneuron as mean ± SD, $n = 6$; one-way ANOVA, $P > 0.05$ for control vs. d-tubocurarine; $P > 0.05$ for d-tubocurarine vs. $Cd^{2+}$. Each dot represents the data from single neurons. (*D*) Reconstruction of the two recorded esV2a interneurons (*Upper*). (*Lower*) Coexpression of VAChT (green) and Cx36 (red and indicated by a white arrow) at the crossing point of their axons (blue) that represents the presumed site of contact located in the segment of the caudal esV2a interneuron. These images correspond to the region indicated in the box of the *Upper* panel. The axon of esV2a interneurons is indicated by the dashed lines. (*E*) Triple whole-cell patch-clamp recordings from two rostral esV2a interneurons and a pMN. Each esV2a interneuron produced subthreshold EPSPs in the pMN, which was recruited by the convergent input from the two interneurons. Two superimposed traces are shown to indicate the reliability of firing and variability in spike amplitude. Black arrows indicate the peaks of two spikes. (*F*) Quantification of the mean EPSP amplitude induced in pMNs by each esV2a interneuron. The graph represents mean ± SD, $n = 13$; paired *t* test, $P = 0.8 \times 10^{-4}$. Each dot represents the data from a single neuron.

when the two esV2a interneurons were simultaneously stimulated, there was a synaptic summation of the excitatory responses that elicited reliable action potential firing by the pMN (Fig. 6 *E* and *F*). Thus, the convergence of a minimum of two esV2a interneurons was sufficient to recruit pMNs.

**Reciprocal Connections between esV2a Interneurons and CoLo Interneurons.** SBEM data revealed that CoLo interneurons receive inputs via chemical synapses from esV2a interneurons and in turn provide synaptic inputs to contralateral esV2a interneurons and pMNs. These synaptic connections were functionally confirmed using dual whole-cell patch-clamp recordings (Fig. 7). We first recorded a rostral esV2a interneuron and an ipsilateral CoLo interneuron. esV2a interneurons formed both chemical and electrical synapses with CoLo interneurons ($n = 7$) (Fig. 7 *A* and *B*). Stimulation of esV2a interneurons induced EPSPs/EPSCs in CoLo interneurons whose transmitter-mediated component was blocked by d-tubocurarine (50 µM), leaving only an eEPSP, which persisted in $Cd^{2+}$ (100 µM; $n = 7$) (Fig. 7 *A*–*D*). The amplitude of the cEPSP was highest to CoLo interneurons present in the same segment as the activated esV2a interneuron (*SI Appendix*, Fig. S8 *C* and *D*). The recorded pairs of neurons were intracellularly filled with neurobiotin for morphological and immunohistochemical analysis. Zones of presumed synaptic contacts were located between axons of esV2a and CoLo interneurons, and colocalized with VAChT and connexin 36 ($n = 3$ of 3 preparations) (Fig. 7*E*). Conversely, CoLo interneurons provide inhibitory synaptic inputs to esV2a interneurons located on the contralateral side of the spinal cord. Stimulation of a single CoLo interneuron induced inhibitory postsynaptic currents (IPSCs) in a simultaneously recorded contralateral esV2a interneuron that was completely blocked by strychnine (5 µM; $n = 6$) (Fig. 7 *F* and *G*). The reconstruction of the recorded neurons filled with neurobiotin showed axo-axonic close contacts that colocalized with immunoreactivity for the glycine transporter 2 (Glyt2) (Fig. 7*H*).

These results show a circuit with feedforward excitation between the excitatory esV2a and inhibitory commissural CoLo interneurons. Activation of CoLo interneurons in turn provides forward inhibition not only to contralateral pMNs, but also to esV2a interneurons on the contralateral side, which prevents activation of contralateral axial muscles during ipsilateral bending, hence ensuring the directionality of escape.

## Discussion

Vertebrates are endowed with a diverse behavioral repertoire from which a given motor action is selected and executed

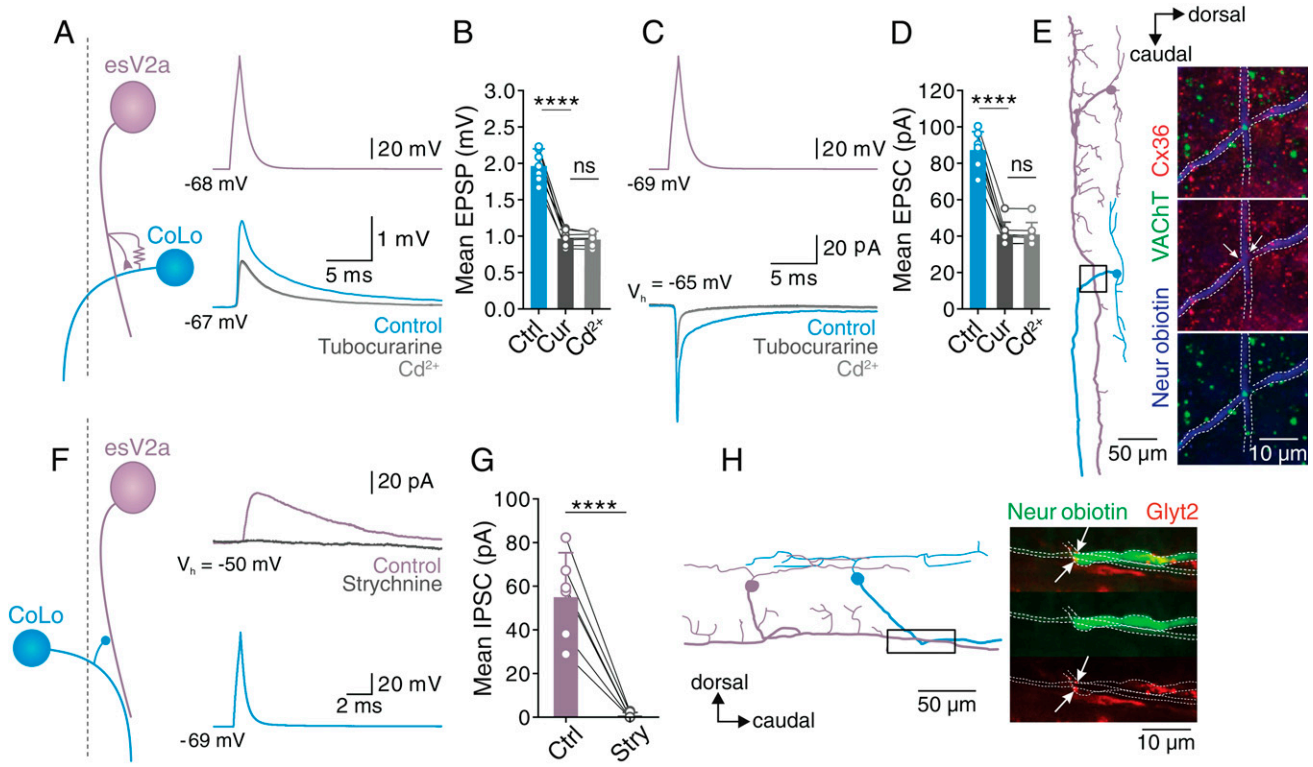


**Fig. 7.** Feedforward excitation and inhibition between esV2a interneurons and CoLo interneurons, respectively. (*A*) Dual whole-cell patch-clamp recording from a rostral esV2a interneuron and an ipsilateral caudal CoLo interneuron (the dashed line indicates the middle line of spinal cord). esV2a interneurons made mixed electrical and chemical synapses with CoLo interneurons. (*B*) Quantification of the mean amplitude of monosynaptic EPSPs in CoLo interneurons. The graph shows mean ± SD, $n = 7$; one-way ANOVA, $P = 7.5 \times 10^{-5}$ for control vs. d-tubocurarine; $P > 0.05$ for d-tubocurarine vs. $Cd^{2+}$. (*C*) The same pair of esV2a interneuron and CoLo interneuron as in *A* in which EPSCs were examined. (*D*) Quantification of the mean amplitude of the monosynaptic EPSCs elicited in CoLo interneurons. Graph represents mean ± SD, $n = 7$; one-way ANOVA, $P = 8.2 \times 10^{-5}$ for control vs. d-tubocurarine; $P > 0.05$ for d-tubocurarine vs. $Cd^{2+}$. Each dot represents the data from single neurons. (*E*) Reconstruction of a recorded esV2a interneuron and CoLo interneuron (*Left*). Confocal image showing the coexpression of VAChT (green) and Cx36 (red and indicated by white arrows) at the site of synaptic contacts between the axons of the two interneurons (blue and indicated by the dashed lines). These images correspond to the region indicated in the box of the *Left* panel. (*F*) Dual whole-cell patch-clamp recording of an esV2a interneuron and a contralateral CoLo interneuron (the dashed line indicates the middle line of spinal cord). Single action potentials in CoLo interneuron elicited IPSCs in esV2a interneuron that were blocked by strychnine. (*G*) Quantification of the effect of strychnine on the mean amplitude of monosynaptic IPSCs. Data are presented as mean ± SD, $n = 6$; paired *t* test, $P = 6.3 \times 10^{-7}$. Each dot represents the data from a single neuron. (*H*) Lateral view of the reconstruction of the pair of CoLo and esV2a interneuron shown in *F*. GlyT2 was expressed at the site of presumed synaptic contact between CoLo and esV2a interneuron axon (arrows).

depending on the circumstances (2, 3, 52, 53). Urgent tasks, such as defensive escape, require circuits that have evolved to provide an almost immediate transformation of commands into motor action, while avoiding the loss of valuable time associated with resolving competing behaviors. In this study, we reveal a specialized spinal circuit relying on strong axo-axonic synaptic connections that plays a pivotal role in action direction implementation during escape in adult zebrafish. A central component of this circuit is a unique, segmentally repeating cholinergic esV2a interneuron expressing the transcription factor Chx10. These interneurons are the first and primary responder to escape commands from M-cells. They play a pivotal role in amplifying and distributing the escape commands through a feedforward circuit via axo-axonic mixed electrical and chemical synapses to all elements of the escape circuit in the spinal cord. The axo-axonic organization of synaptic connections within this circuit likely enables a rapid input–output transformation of command within this circuit. The combined features of the spinal circuit revealed in this study ensure the implementation of the escape behavior and control its directionality.

Escape behavior has historically been considered as a highly stereotyped behavior with an intrinsic lack of flexibility, and hence was thought to involve a relatively simple circuit (12, 33, 54–56). In this early view, activation of M-cells provides a direct and strong excitation to fMNs to produce the body bend during escape (32, 33, 42). Subsequent studies have shown that animals have much more control over the extent of the bend and trajectory of escape (33, 57–59), suggesting a more sophisticated circuit organization beyond a direct control of fMNs from M-cells. Indeed, previous studies revealed that activation of M-cells induced a depolarization of pMNs containing multiple components (32). These components have been suggested to arise from activation of the so-called spinal descending interneurons that provide a powerful excitation to pMNs (33). Furthermore, the amplitude and directionality of the escape behavior can be modulated by local sensory inputs in the spinal cord (27, 30, 60–62).

The specialized cholinergic interneurons identified in our study differ from the so-called descending spinal interneurons described in goldfish. These latter interneurons were shown to be excited exclusively via chemical synapses from M-cells and in turn make electrical coupling with pMNs via contact on their soma and dendrites (32, 33). However, their genetic and transmitter identity and their functional role during escape behavior have not been examined. In contrast, esV2a interneurons revealed in adult zebrafish use axo-axonic mixed chemical and electrical synaptic contacts with pMNs and fMNs, as well as

CoLo interneurons to spread escape commands from M-cells and direct escape behavior in vivo. These cholinergic interneurons also represent a specialized type of V2a interneurons that differ from those driving swimming (34, 39–41). The latter are glutamatergic, have long axonal projections, and make synaptic contacts with dendrites and soma of motor neurons (41).

By combining dual or triple intracellular recordings from the constituent neurons and SBEM technology (47–50), we constructed a detailed synapse-resolution functional connectivity map of this escape circuit. A segmentally repeating cholinergic esV2a interneuron expressing Chx10 represents a central player of this circuit. These interneurons rely on axo-axonic synaptic connections and feedforward excitation to immediately transform M-cell commands into rapid and unidirectional escape behavior. The esV2a interneurons are the only neurons within the spinal escape circuit to receive direct, mixed chemical, and electrical excitation from M-cells. They then amplify and deliver the excitation via a feedforward circuit to other esV2a interneurons as well as to pMNs, fMNs, and CoLos. Ablation of esV2a eliminated the implementation of escape behavior toward the ablated side in vivo. Thus, our results reveal the molecular identity of a specialized excitatory interneuron class, their segmental distribution and transmitter identity, their interconnectivity, their feedforward axo-axonic connections with motor neurons and commissural interneurons, and their behavioral relevance for implementing escape behavior and controlling body trajectory. This study demonstrates local circuit mechanisms within the spinal cord that control the extent of the C-shape bend and direct the trajectory of escape behavior, and hence provides a mechanism for flexible trajectory to move away from a threat in the living animal.

In vertebrates, action selection is often considered to be the realm of higher cognitive processing, while the implementation of the selected action is assigned to brainstem–spinal circuits. Interactions between many circuits in the brain, especially the basal ganglia, have been linked to selection for purposive motor actions (1, 7–9, 63). However, the evaluative processing involved in the selection of a specific motor behavior, or sequences of actions, would be incompatible for urgent tasks such as escape: any time lost resolving conflicts with competing behaviors would result in fatal errors. Both in mammals and fish the commands for urgent behaviors, such as predation and escape, seem to be processed by circuits independent of the basal ganglia (10–13). For example, in zebrafish, the balance of excitation between M-cells is controlled by feedforward inhibition from local neurons and this can contribute to the initial selection of which side is activated during escape (17, 29). Modulator circuits in the brain also contribute to mediating a more flexible escape behavior (19, 20, 64–68). Our results now demonstrate an additional layer of processing at the spinal cord level that not only transforms escape commands into motor action, but could provide an additional level of computation that could take into account spinal local inputs to determine the extent of the escape movement and control its trajectory. For example, local excitatory sensory inputs could act either directly or via local inhibitory interneurons (30) to change the excitability of esV2a interneurons, and thereby influence escape. Studies in invertebrates have shown that computation within local circuits mediate selection and switching between different motor programs (69–74). Thus, in vertebrates, the standard view of the mechanisms of direction selectivity needs to include local spinal circuits that can implement motor actions and direct their trajectory.

## Materials and Methods

**Animals.** Zebrafish (*Danio rerio*) were raised and maintained with an automatic fish-housing system in a zebrafish facility at the Tongji University and Karolinska Institute according to established procedures. All the experimental protocols were approved by the Animal Use Committee of Tongji University and the Animal Research Ethical Committee in Stockholm and were performed in accordance with regulation in China and with European Union guidelines. Details of the transgenic lines are given in *SI Appendix*.

**Immunohistochemistry.** To reveal the identity of esV2a interneurons, spinal cords were dissected out after 24-h fixation. The tissue was then processed for multiple immunohistochemical labeling against GFP (Abcam), Chx10 (75), and ChAT (76). Details are given in *SI Appendix*.

**Electrophysiology.** The brain–spinal cord was dissected out and transferred to a recording chamber that was continuously perfused with an extracellular solution (43, 44). Whole-cell patch-clamp recordings were performed from $GFP^+$ neurons or retrogradely labeled MNs in the Tg(*Chx10*:GFP) (34) or Tol-056 fish line (42). Details are given in *SI Appendix*.

**SBEM Imaging and Neurite Reconstruction.** The SBEM image acquisition was performed on a field-emission scanning electron microscope (Gemini 300, Zeiss) equipped with an in-chamber ultramicrotome (3ViewXP, Gatan) using a back-scattered electron detector (Onpont, Gatan). Serial images (18,000 × 14,000 pixels) of 12-nm pixel size were acquired with a nominal cutting thickness of 35 nm. Incident beam energy was 2 keV and the dwell time 1.5 μs. In total, 7,095 slices were collected, resulting in a three-dimensional volume of $251.4 \times 187.7 \times 248.3\ \mu m^3$). Details are given in *SI Appendix*.

**Laser Ablation of GFP-Labeled Interneurons.** To perform laser ablation in ex vivo brain–spinal cord preparations, a two-photon laser (Coherent laser Ultra II) operating at an 80-MHz repetition-rate with a <140-fs pulse duration was used with a microscope (Scientifica) equipped with IR-differential interference contrast optics and a CCD camera with frame grabber (QIMAGING) to target and ablate specifically spinal esV2a interneurons. Details are given in *SI Appendix*.

**In Vivo Behavioral Analysis.** In vivo behavioral analysis details are given in *SI Appendix*.

**Data Analysis.** Data analysis details are given in *SI Appendix*.

**Data Availability.** The raw data supporting this study are publicly available at https://wklink.org/6271. All annotations and codes used for analysis are available upon publication at http://www.shipm.cn/jyjz_web/html/jyjz_English/jyjz_eg_hyf_kycg/List/list_0.htm.

**ACKNOWLEDGMENTS.** We thank Drs. M. Bertuzzi, S. Grillner, L. Picton, and G. Silberberg for comments on the manuscript; Drs. J.-L. Du and S. Higashijima for sharing the fish lines; X. Wang and X. Ding, Shanghai Jiao Tong University School of Medicine, for helping acquiring and analyzing the electron microscopy data; and J. Mao and S. Kisana for fish care. This work was supported by the National Key Research and Development Program of China (2018YFA0108000); Shanghai Municipal Science and Technology Major Project (2018SHZDZX05); National Natural Science Foundation of China (31771168, 81811530025, 31972904, 31900706, 81901261); Natural Science Foundation of Shanghai (20ZR1472500); the 2017 Thousand Youth Talents Plan of China (J.S.); Shanghai Blue Cross Brain Hospital Co., Ltd. and Shanghai Tongji University Education Development Foundation; Program for Professor of Special Appointment (Eastern Scholar) at Shanghai Institutions of Higher Learning QD2018015 (to Y.H.); the Swedish Research Council (2017-02905); the Wallenberg Foundation (KAW 2018.0010); Swedish Brain Foundation (FO2021-0317); and the Karolinska Institute (A.E.M.).

1. A. Klaus, J. Alves da Silva, R. M. Costa, What, if, and when to move: Basal ganglia circuits and self-paced action initiation. *Annu. Rev. Neurosci.* **42**, 459–483 (2019).
2. S. Arber, R. M. Costa, Connecting neuronal circuits for movement. *Science* **360**, 1403–1404 (2018).
3. S. Grillner, A. El Manira, Current principles of motor control, with special reference to vertebrate locomotion. *Physiol. Rev.* **100**, 271–320 (2020).
4. M. Murakami, Z. F. Mainen, Preparing and selecting actions with neural populations: Toward cortical circuit mechanisms. *Curr. Opin. Neurobiol.* **33**, 40–46 (2015).
5. O. Hikosaka, Neural systems for control of voluntary action—A hypothesis. *Adv. Biophys.* **35**, 81–102 (1998).
6. I. S. Grunfeld, E. Likhtik, Mixed selectivity encoding and action selection in the prefrontal cortex during threat assessment. *Curr. Opin. Neurobiol.* **49**, 108–115 (2018).

7. A. M. Graybiel, S. T. Grafton, The striatum: Where skills and habits meet. *Cold Spring Harb. Perspect. Biol.* **7**, a021691 (2015).
8. S. Grillner, B. Robertson, The basal ganglia over 500 million years. *Curr. Biol.* **26**, R1088–R1100 (2016).
9. R. Amo *et al.*, The habenulo-raphe serotonergic circuit encodes an aversive expectation value essential for adaptive active avoidance of danger. *Neuron* **84**, 1034–1048 (2014).
10. K. Lingenhöhl, E. Friauf, Giant neurons in the rat reticular formation: A sensorimotor interface in the elementary acoustic startle circuit? *J. Neurosci.* **14**, 1176–1194 (1994).
11. R. Gómez-Nieto *et al.*, Origin and function of short-latency inputs to the neural substrates underlying the acoustic startle reflex. *Front. Neurosci.* **8**, 216 (2014).
12. D. S. Faber, J. R. Fetcho, H. Korn, Neuronal networks underlying the escape response in goldfish. General implications for motor control. *Ann. N. Y. Acad. Sci.* **563**, 11–33 (1989).
13. Y. Mu, X. Q. Li, B. Zhang, J. L. Du, Visual input modulates audiomotor function via hypothalamic dopaminergic neurons through a cooperative mechanism. *Neuron* **75**, 688–699 (2012).
14. E. A. Naumann *et al.*, From whole-brain data to functional circuit models: The zebrafish optomotor response. *Cell* **167**, 947–960.e20 (2016).
15. J. M. Cregg *et al.*, Brainstem neurons that command mammalian locomotor asymmetries. *Nat. Neurosci.* **23**, 730–740 (2020).
16. K. H. Huang, M. B. Ahrens, T. W. Dunn, F. Engert, Spinal projection neurons control turning behaviors in zebrafish. *Curr. Biol.* **23**, 1566–1573 (2013).
17. M. Koyama *et al.*, A circuit motif in the zebrafish hindbrain for a two alternative behavioral choice to turn left or right. *eLife* **5**, e16808 (2016).
18. H. Korn, D. S. Faber, The Mauthner cell half a century later: A neurobiological model for decision-making? *Neuron* **47**, 13–28 (2005).
19. K. Bhattacharyya, D. L. McLean, M. A. MacIver, Visual threat assessment and reticulospinal encoding of calibrated responses in larval zebrafish. *Curr. Biol.* **27**, 2751–2762.e6 (2017).
20. T. W. Dunn *et al.*, Neural circuits underlying visually evoked escapes in larval zebrafish. *Neuron* **89**, 613–628 (2016).
21. J. C. Liao, J. R. Fetcho, Shared versus specialized glycinergic spinal interneurons in axial motor circuits of larval zebrafish. *J. Neurosci.* **28**, 12982–12992 (2008).
22. S. A. Budick, D. M. O'Malley, Locomotor repertoire of the larval zebrafish: Swimming, turning and prey capture. *J. Exp. Biol.* **203**, 2565–2579 (2000).
23. P. Domenici, M. E. Hale, Escape responses of fish: A review of the diversity in motor control, kinematics and behaviour. *J. Exp. Biol.* **222**, jeb166009 (2019).
24. T. Kohashi, Y. Oda, Initiation of Mauthner- or non-Mauthner-mediated fast escape evoked by different modes of sensory input. *J. Neurosci.* **28**, 10641–10653 (2008).
25. K. S. Liu, J. R. Fetcho, Laser ablations reveal functional relationships of segmental hindbrain neurons in zebrafish. *Neuron* **23**, 325–335 (1999).
26. D. M. O'Malley, Y. H. Kao, J. R. Fetcho, Imaging the functional organization of zebrafish hindbrain segments during escape behaviors. *Neuron* **17**, 1145–1155 (1996).
27. J. Song, K. Ampatzis, J. Ausborn, A. El Manira, A hardwired circuit supplemented with endocannabinoids encodes behavioral choice in zebrafish. *Curr. Biol.* **25**, 2610–2620 (2015).
28. M. Koyama, A. Kinkhabwala, C. Satou, S. Higashijima, J. Fetcho, Mapping a sensory-motor network onto a structural and functional ground plan in the hindbrain. *Proc. Natl. Acad. Sci. U.S.A.* **108**, 1170–1175 (2011).
29. T. Shimazaki, M. Tanimoto, Y. Oda, S. I. Higashijima, Behavioral role of the reciprocal inhibition between a pair of Mauthner cells during fast escapes in zebrafish. *J. Neurosci.* **39**, 1182–1194 (2019).
30. Y. C. Liu, M. E. Hale, Local spinal cord circuits and bilateral Mauthner cell activity function together to drive alternative startle behaviors. *Curr. Biol.* **27**, 697–704 (2017).
31. M. E. Hale, H. R. Katz, M. Y. Peek, R. T. Fremont, Neural circuits that drive startle behavior, with a focus on the Mauthner cells and spiral fiber neurons of fishes. *J. Neurogenet.* **30**, 89–100 (2016).
32. J. R. Fetcho, D. S. Faber, Identification of motoneurons and interneurons in the spinal network for escapes initiated by the Mauthner cell in goldfish. *J. Neurosci.* **8**, 4192–4213 (1988).
33. J. R. Fetcho, Excitation of motoneurons by the Mauthner axon in goldfish: Complexities in a "simple" reticulospinal pathway. *J. Neurophysiol.* **67**, 1574–1586 (1992).
34. Y. Kimura, Y. Okamura, S. Higashijima, alx, a zebrafish homolog of Chx10, marks ipsilateral descending excitatory interneurons that participate in the regulation of spinal locomotor circuits. *J. Neurosci.* **26**, 5684–5697 (2006).
35. E. E. Ljunggren, S. Haupt, J. Ausborn, K. Ampatzis, A. El Manira, Optogenetic activation of excitatory premotor interneurons is sufficient to generate coordinated locomotor activity in larval zebrafish. *J. Neurosci.* **34**, 134–139 (2014).
36. Y. Kimura *et al.*, Hindbrain V2a neurons in the excitation of spinal locomotor circuits during zebrafish swimming. *Curr. Biol.* **23**, 843–849 (2013).
37. E. Eklöf-Ljunggren *et al.*, Origin of excitation underlying locomotion in the spinal circuit of zebrafish. *Proc. Natl. Acad. Sci. U.S.A.* **109**, 5511–5516 (2012).
38. J. R. Sternberg *et al.*, Optimization of a neurotoxin to investigate the contribution of excitatory interneurons to speed modulation in vivo. *Curr. Biol.* **26**, 2319–2328 (2016).
39. K. Ampatzis, J. Song, J. Ausborn, A. El Manira, Separate microcircuit modules of distinct v2a interneurons and motoneurons control the speed of locomotion. *Neuron* **83**, 934–943 (2014).
40. E. Menelaou, D. L. McLean, Hierarchical control of locomotion by distinct types of spinal V2a interneurons in zebrafish. *Nat. Commun.* **10**, 4197 (2019).
41. J. Song, E. Dahlberg, A. El Manira, V2a interneuron diversity tailors spinal circuit organization to control the vigor of locomotor movements. *Nat. Commun.* **9**, 3370 (2018).
42. C. Satou *et al.*, Functional role of a specialized class of spinal commissural inhibitory neurons during fast escapes in zebrafish. *J. Neurosci.* **29**, 6780–6793 (2009).
43. A. Kyriakatos *et al.*, Initiation of locomotion in adult zebrafish. *J. Neurosci.* **31**, 8422–8431 (2011).
44. J. P. Gabriel *et al.*, Principles governing recruitment of motoneurons during swimming in zebrafish. *Nat. Neurosci.* **14**, 93–99 (2011).
45. J. Ausborn, R. Mahmood, A. El Manira, Decoding the rules of recruitment of excitatory interneurons in the adult zebrafish locomotor network. *Proc. Natl. Acad. Sci. U.S.A.* **109**, E3631–E3639 (2012).
46. J. Song *et al.*, Multiple rhythm-generating circuits act in tandem with pacemaker properties to control the start and speed of locomotion. *Neuron* **105**, 1048–1061.e4 (2020).
47. K. M. Boergens *et al.*, webKnossos: Efficient online 3D data annotation for connectomics. *Nat. Methods* **14**, 691–694 (2017).
48. T. J. Deerinck *et al.*, High-performance serial block-face SEM of nonconductive biological samples enabled by focal gas injection-based charge compensation. *J. Microsc.* **270**, 142–149 (2018).
49. Y. Hua, P. Laserstein, M. Helmstaedter, Large-volume en-bloc staining for electron microscopy-based connectomics. *Nat. Commun.* **6**, 7923 (2015).
50. F. N. Svara, J. Kornfeld, W. Denk, J. H. Bollmann, Volume EM reconstruction of spinal cord reveals wiring specificity in speed-related motor circuits. *Cell Rep.* **23**, 2942–2954 (2018).
51. K. Ampatzis, J. Song, J. Ausborn, A. El Manira, Pattern of innervation and recruitment of different classes of motoneurons in adult zebrafish. *J. Neurosci.* **33**, 10875–10886 (2013).
52. O. Kiehn, Decoding the organization of spinal circuits that control locomotion. *Nat. Rev. Neurosci.* **17**, 224–238 (2016).
53. L. Garcia-Campmany, F. J. Stam, M. Goulding, From circuits to behaviour: Motor networks in vertebrates. *Curr. Opin. Neurobiol.* **20**, 116–125 (2010).
54. R. C. Eaton, R. A. Bombardieri, D. L. Meyer, The Mauthner-initiated startle response in teleost fish. *J. Exp. Biol.* **66**, 65–81 (1977).
55. J. Diamond, J. Mellanby, The effect of tetanus toxin in the goldfish. *J. Physiol.* **215**, 727–741 (1971).
56. S. J. Zottoli, Correlation of the startle reflex and Mauthner cell auditory responses in unrestrained goldfish. *J. Exp. Biol.* **66**, 243–254 (1977).
57. R. C. Eaton, R. DiDomenico, J. Nissanov, Flexible body dynamics of the goldfish C-start: Implications for reticulospinal command mechanisms. *J. Neurosci.* **8**, 2758–2768 (1988).
58. R. C. Eaton, D. S. Emberley, How stimulus direction determines the trajectory of the Mauthner-initiated escape response in a teleost fish. *J. Exp. Biol.* **161**, 469–487 (1991).
59. K. R. Svoboda, J. R. Fetcho, Interactions between the neural networks for escape and swimming in goldfish. *J. Neurosci.* **16**, 843–852 (1996).
60. K. Umeda, T. Ishizuka, H. Yawo, W. Shoji, Position- and quantity-dependent responses in zebrafish turning behavior. *Sci. Rep.* **6**, 27888 (2016).
61. S. Knafo *et al.*, Mechanosensory neurons control the timing of spinal microcircuit selection during locomotion. *eLife* **6**, e25260 (2017).
62. T. H. Miller *et al.*, Social status-dependent shift in neural circuit activation affects decision making. *J. Neurosci.* **37**, 2137–2148 (2017).
63. K. Doya, M. N. Shadlen, Decision making. *Curr. Opin. Neurobiol.* **22**, 911–913 (2012).
64. Y. Yao *et al.*, Visual cue-discriminative dopaminergic control of visuomotor transformation and behavior selection. *Neuron* **89**, 598–612 (2016).
65. A. Pujala, M. Koyama, Chronology-based architecture of descending circuits that underlie the development of locomotor repertoire after birth. *eLife* **8**, e42135 (2019).
66. G. D. Marquart, K. M. Tabor, S. A. Bergeron, K. L. Briggman, H. A. Burgess, Prepontine non-giant neurons drive flexible escape behavior in zebrafish. *PLoS Biol.* **17**, e3000480 (2019).
67. I. Temizer, J. C. Donovan, H. Baier, J. L. Semmelhack, A visual pathway for looming-evoked escape in larval zebrafish. *Curr. Biol.* **25**, 1823–1834 (2015).
68. A. M. Lacoste *et al.*, A convergent and essential interneuron pathway for Mauthner-cell-mediated escapes. *Curr. Biol.* **25**, 1526–1534 (2015).
69. C. R. von Reyn *et al.*, A spike-timing mechanism for action selection. *Nat. Neurosci.* **17**, 962–970 (2014).
70. D. M. Blitz, M. P. Nusbaum, Neural circuit flexibility in a small sensorimotor system. *Curr. Opin. Neurobiol.* **21**, 544–552 (2011).
71. S. W. Flavell *et al.*, Serotonin and the neuropeptide PDF initiate and extend opposing behavioral states in *C. elegans*. *Cell* **154**, 1023–1035 (2013).
72. Q. Gaudry, W. B. Kristan Jr., Behavioral choice by presynaptic inhibition of tactile sensory terminals. *Nat. Neurosci.* **12**, 1450–1457 (2009).
73. S. Faumont, T. H. Lindsay, S. R. Lockery, Neuronal microcircuits for decision making in *C. elegans*. *Curr. Opin. Neurobiol.* **22**, 580–591 (2012).
74. B. K. Shaw, W. B. Kristan, Jr, The neuronal basis of the behavioral choice between swimming and shortening in the leech: Control is not selectively exercised at higher circuit levels. *J. Neurosci.* **17**, 786–795 (1997).
75. Y. Kimura, C. Satou, S. Higashijima, V2a and V2b neurons are generated by the final divisions of pair-producing progenitors in the zebrafish spinal cord. *Development* **135**, 3001–3005 (2008).
76. A. Pedroni, K. Ampatzis, Large-scale analysis of the diversity and complexity of the adult spinal cord neurotransmitter typology. *iScience* **19**, 1189–1201 (2019).